Differentiation of Myositis-Induced Models of Bacterial Infection and Inflammation with T_2-Weighted, CEST, and DCE-MRI

Joshua M. Goldenberg[1,2], Alexander J. Berthusen[3], Julio Cárdenas-Rodríguez[4], and Mark D. Pagel[5]

[1]Department of Pharmaceutical Sciences, University of Arizona, Tucson, AZ; [2]Department of Genitourinary Medical Oncology, The University of Texas MD Anderson Cancer Center, Houston, TX; [3]Department of Ecology and Evolutionary Biology, University of Arizona, Tucson, AZ; [4]Banner University Medical Center, University of Arizona, Tucson, AZ; and [5]Department of Cancer Systems Imaging, The University of Texas MD Anderson Cancer Center, Houston, TX

Corresponding Author:
Mark D. Pagel, PhD
Department of Cancer Systems Imaging, MD Anderson Cancer Center, 3SCR4.3642, Unit 1907, Houston, TX 77054-1901,
E-mail: mdpagel@mdanderson.org

Key Words: imaging infection, principal components analysis, T_2-weighted MRI, CEST-MRI, DCE-MRI, machine learning

Abbreviations: Chemical exchange saturation transfer (CEST), dynamic contrast-enhanced (DCE), magnetic resonance imaging (MRI), area under the curve (AUC), principal component analysis (PCA), positron emission tomography (PET), magnetic resonance (MR), repetition time (TR), echo time (TE), field of view (FOV), regions of interest (ROIs), contrast-to-noise ratio (CNR), receiver operating curve (ROC), hematoxylin and eosin (H&E)

ABSTRACT

We used T_2 relaxation, chemical exchange saturation transfer (CEST), and dynamic contrast-enhanced (DCE) magnetic resonance imaging (MRI) to assess whether bacterial infection can be differentiated from inflammation in a myositis-induced mouse model. We measured the T_2 relaxation time constants, %CEST at 5 saturation frequencies, and area under the curve (AUC) from DCE-MRI after maltose injection from infected, inflamed, and normal muscle tissue models. We applied principal component analysis (PCA) to reduce dimensionality of entire CEST spectra and DCE signal evolutions, which were analyzed using standard classification methods. We extracted features from dimensional reduction as predictors for machine learning classifier algorithms. Normal, inflamed, and infected tissues were evaluated with H&E and gram-staining histological studies, and bacterial-burden studies. The T_2 relaxation time constants and AUC of DCE-MRI after injection of maltose differentiated infected, inflamed, and normal tissues. %CEST amplitudes at −1.6 and −3.5 ppm differentiated infected tissues from other tissues, but these did not differentiate inflamed tissue from normal tissue. %CEST amplitudes at 3.5, 3.0, and 2.5 ppm, AUC of DCE-MRI for shorter time periods, and relative K^{trans} and k_{ep} values from DCE-MRI could not differentiate tissues. PCA and machine learning of CEST-MRI and DCE-MRI did not improve tissue classifications relative to traditional analysis methods. Similarly, PCA and machine learning did not further improve tissue classifications relative to T_2 MRI. Therefore, future MRI studies of infection models should focus on T_2-weighted MRI and analysis of T_2 relaxation times.

INTRODUCTION

The diagnosis and treatment of bacterial infections remain a central problem in medicine. For example, bacterial infections have a higher annual mortality than AIDS, breast cancer, and prostate cancer combined (1). In addition, the medical burden generated from infections is expected to rise in the next two decades, owing to antibacterial resistance and the anticipated increase in the number of patients receiving implanted medical devices (2-5). Some progress has been made in identifying bacterial infections by means of computed tomography and positron emission tomography (PET). Radiotracers used for these methods lack the capability of measuring symptoms consistent with bacterial infections. However, the specificity of bacterial imaging has improved with the synthesis of radiotracers with a high translational potential (6-8) which make the utility of these methods capable of measuring the presence of bacteria (9).

Creative applications of standard magnetic resonance imaging (MRI) methods may improve the specificity of diagnosing infection and inflammation. Small animal models are widely studied to translationally implement noninvasive imaging of bacterial infections and inflammation (10-11). For example, T_2-weighted MRI can be used to differentiate between benign and malignant inflammatory breast lesions (12). In addition, T_2-weighted MRI can help identify the presence of bacterial infections arising from methicillin-sensitive *Staphylococcus aureus* (13) or viral infections such as Zika and Cytomegalovirus (14-15). A temporal series of dynamic contrast enhanced (DCE) magnetic resonance (MR) images can be used to measure transport rate constants and identify inflammation caused by atherosclerotic plaques (16-19). A series of chemical exchange saturation transfer (CEST) MR images can be used to noninvasively measure quantitative %CEST values for longi-

ISSN 2379-1381 https://doi.org/10.18383/j.tom.2019.00009

tudinal monitoring of bacterial brain abscesses (20), and bacteriolytic cancer therapy (21).

Principal component analysis (PCA) is a widely available and viable tool that can address the plethora of multifaceted information contained in MR data sets such as numerous images with different TE times for T_2 MRI, different time points for DCE-MRI, and different saturation frequencies for CEST-MRI (22-24). The combination of PCA and machine learning can potentially improve the classification of the pathological condition with T_2 MRI, DCE-MRI, and CEST-MRI.

We sought to test the efficacy of MRI studies with a small animal model of myositis-induced infection to differentiate bacterial infection from inflammation and differentiate infected or inflamed tissue from normal tissues. In particular, we established distinct tissue models by inoculating *Escherichia coli* into the right thigh, and heat-killed, inactivated *E. coli* into the left thigh of each mouse. We hypothesized that T_2 MRI would be sufficient to differentiate these tissue models given the difference in T_2 relaxation times between normal muscle, inflamed muscle, and infected muscle (25-26). We also hypothesized that differences between the inflamed and infected tissue models could be detected by CEST-MRI (27-30). A final objective of our study was to determine if the T_2-exchange (T_{2ex}) contrast agent maltose could be used for DCE-MRI. Unlike bacterial cells, mammalian cells do not contain the necessary cellular machinery for the processing of maltodextrins for energy production (31-34). Therefore, bacterial infection may differ from inflammation with regard to the dynamic uptake of maltose.

METHODOLOGY

In Vivo Studies

All animals were cared for in compliance with protocols approved by the Institutional Animal Care and Use Committee of the University of Arizona. Twenty, 4- to 6-week-old female immunocompetent CBA/J mice were inoculated with $\sim 5 \times 10^7$ CFU/mL *E. coli* (ATCC 25922) in the right thigh muscle, and $\sim 5 \times 10^7$ CFU/mL heat-inactivated *E. coli* in the left thigh muscle, 6-12 h before imaging. In addition, 5 CBA/J mice were immunosuppressed with cyclophosphamide treatment (MP Biomedicals; Santa Ana, CA), with 150 mg/kg administered intraperitoneally 5 days before imaging, and 100 mg/kg administered 1 day before imaging. Before the MRI scan, each mouse was anesthetized with 1.5%–2.5% isoflurane in O_2 carrier gas, and a 27 G catheter was placed in the tail vein. Physiologic respiration rate and core body temperature were monitored throughout the MRI session. All animals were imaged while maintaining their temperature at 37.0°C ± 0.2°C using warm air controlled by a temperature feedback system (SA Instruments, NY).

In Vivo T_2 MRI

We performed T_2-weighted spin-echo MRI to localize the myositis-induced thigh and the contralateral inflamed thigh, which required 3.3 minutes to acquire (Figure 1A, left). The T_2 relaxation time of all tissues was measured using a multi-slice multi-echo (MSME) acquisition method with a variable echo spacing as follows: repetition time (TR) = 3.0 seconds; echo time (TE) = 10, 20, 30, 40, 50, 60, 70, 80, 90, 100, 110, and 120 milliseconds; average = 1; linear encoding order; field of view (FOV) = 6.0 × 4.0 cm^2; slice thickness = 1.0 mm; matrix = 128 × 128; for 5 slices centered on the site of infection; in-plane spatial resolution = 0.47 × 0.31 mm^2; scan time = 6.4 minutes (Figure 1C). The signal profiles from the regions of interest (ROIs) that represented the four tissue classes (Figure 1A, right) were fit with a monoexponential function without a constant offset using least square curve fitting to estimate the T_2 relaxation time.

In Vivo CEST-MRI

Endogenous CEST-MRI studies were performed with a respiration-gated CEST-Fast Imaging with Steady-State Precession (CEST-FISP) MRI acquisition protocol with the following parameters: TR = 3.7 milliseconds; TE = 1.7 milliseconds; averages = 4; excitation pulse angle = 15°; centric encoding order; unbalanced "FID" mode; slice thickness = 1.0 mm; FOV = 6.0 × 4.0 cm^2; in-plane spatial resolution = 0.47 × 0.31 mm^2; matrix = 128 × 128; acquisition time = 453 milliseconds (35). A saturation period was applied before each FISP acquisition, consisting of 1 continuous-wave radiofrequency pulse of 3.0 seconds at a saturation power of 1.0 μT, with no additional spoiling and fat saturation pulses. Selective saturation was applied at 110 frequencies ranging from −55 to −50 ppm in increments of 0.625 ppm (9 frequencies); and −8 to 8 ppm in increments of 0.16 ppm (101 frequencies), which required a total of 25 minutes. CEST spectra from the ROI of the tumor were fit with a sum of 6 Lorentzian line shapes to measure %CEST at 3.5, 3.0, 2.0, −1.6, and −3.5 ppm, and to account for direct saturation of water at 0 ppm (Figure 1B) (36).

In Vivo DCE-MRI

A series of T_2-weighted DCE-MR images were acquired using a spin-echo MRI protocol with TR = 250 milliseconds; echo train length = 10 milliseconds; effective TE = 10 milliseconds; averages = 4; repetitions = 32; FOV = 6 × 4 cm^2; in-plane spatial resolution = 0.94 × 0.63 mm^2; linear encoding order; matrix = 64 × 64; slice thickness = 1.0 mm, for 5 slices centered in the site of infection (Figure 1D). Each individual rapid acquisition with relaxation enhancement (RARE) image was acquired in 64 seconds, and repeated 32 times. An initial set of baseline images was acquired for 10.7 minutes (10 scans) before intravenous injection of 3.0 mmol/kg D-maltose solution (Sigma-Aldrich, St. Louis, MO) and subsequent infusion of contrast agent at a rate of 400 μL/h for the remaining 23.5 minutes, for a total scan time of 34.1 minutes. A 50-μL bolus of 0.5M Multihance® (Bracco Imaging, Milan, Italy) was injected at the end of each imaging session to confirm successful catheterization, which delivered 1.0 mmol/kg of the agent to the mouse. The DCE-MRI signal of the ROIs were first normalized to the average baseline signal before injection of D-maltose, and then divided by the standard deviation of noise (measured from a region of the image that represented air) to obtain a contrast-to-noise ratio (CNR), and then thresholded at $\geq 2\sqrt{2}$ CNR to ensure that only real contrast was analyzed. The area under the curve (AUC) was calculated from the time of injection to 2 minutes, from injection to 5 minutes, from injection to 17 minutes, and from injection to 22 minutes. The DCE-MRI results were also analyzed with the linear reference region model to estimate the relative K^{trans} and k_{ep} values for each ROI (37).

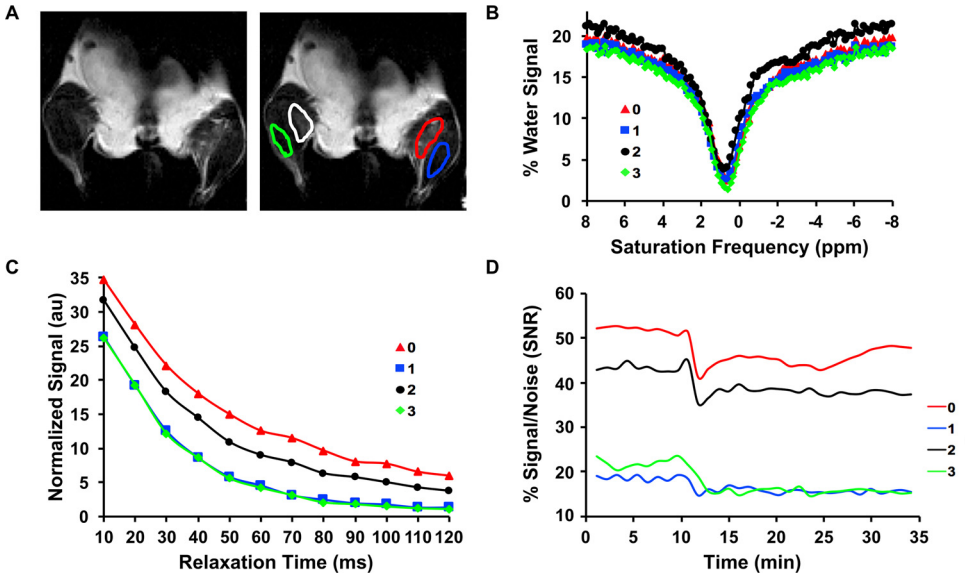

Figure 1. Imaging results for in vivo mouse studies. Throughout the figure, the infected tissue class (0) is shown in red; the normal muscle on left thigh tissue class (1) is shown in blue; the inflamed tissue class (2) is shown in white or black; and the normal muscle on right thigh tissue class (3) is shown in green. Example of a T_2-weighted anatomical image of a myositis-induced mouse (left), and the same mouse with an example of tissue ROIs selected for analysis (right) (A). Examples of chemical exchange saturation transfer (CEST) spectra for the 3 tumor models (B). Examples of T_2-weighted signal decay curves for the 4 tissue models (C). Examples of dynamic contrast-enhanced (DCE) contrast-to-noise ratio (CNR) evolutions for the 4 tissue models (D).

Analysis Methods

All analyses of T_2 MRI, CEST-MRI, and DCE-MRI results were completed with MATLAB 2017b (MathWorks, Inc., Natick, MA). Boxplots were constructed for average T_2 relaxation time, %CEST at specific saturation frequencies, and AUC of DCE-MRI for each tumor model using RStudio (RStudio, Inc., Boston, MA) and Rattle (Togaware, Canberra, Australia) (Figure 2). These boxplots showed the median of each tumor model as a thick horizontal line, 95% confidence intervals of the median as notches, 25% and 75% quartiles as thin horizontal lines, open circles as data points that are beyond the interquartile ranges, and vertical dashed lines as the range. Groups were considered to be different when a Wilcoxon rank-sum analysis showed $P \leq .05$ between groups.

Three analysis methods were used to build tumor classification models with the T_2 relaxation times (Figure 1C and Figure 3), CEST spectra (Figure 1B and Figure 4), and DCE CNR evolutions (Figure 1D and Figure 5). A 30-fold cross-validation method was used to prevent overfitting the model. The performance of each model was measured using the AUC of the receiver operating curve (ROC). In addition, predictive classification models were assessed to evaluate true-positive rates versus false-negative rates, and positive predictive values versus false discovery rates (true-positive and false-positive rates for classifications). The support vector machine (SVM) classification using T_2 relaxation times was performed with 1 PCA component that explained 95% variance of the data, a 1-vs-1 multiclass method, box constraint = 2, and kernel scale = 3.2. Training required 2.33 seconds and the prediction speed was ~690 observations/s. The k-nearest neighbor classification of CEST spectra was performed with 5 PCA components, a one-vs-one multiclass method, 3 neighbors, a cosine distance metric, and equal distance weight. Training required 0.904 seconds, and the prediction speed was ~220 observations/s. The k-nearest neighbor classification of DCE CNR evolutions was performed with 5 PCA components, a 1-vs-1 multiclass method, 10 neighbors, cosine distance metric, and equal distance weight. Training required 0.667 seconds, and the prediction speed was ~310 observations/s. Linear discriminant analysis, subspace discriminant analysis, medium tree, and random forest machine learning algorithms were also used for classification using T_2 relaxation times, CEST spectra, and DCE CNR evolutions.

Histology

Six, 6- to 8-week-old female immunocompetent CBA/J mice were analyzed with hematoxylin and eosin (H&E) and Gram staining studies (The Jackson Laboratory; Bar Harbor, ME). The mice were each inoculated with ~5×10^7 CFU/mL *E. coli* in the right thigh. Inflammation in the left thigh of two mice in one group was induced by means of intramuscular administration of ~5×10^7 CFU/mL heat-inactivated *E. coli*. In another group of two mice, 750 μg/100 g of 10 mg/mL lipopolysaccharide (LPS) from *E. coli* O111:B4 (Sigma Aldrich; St. Louis, MO, USA) was intramuscularly administered. Two mice in the third group were treated with intramuscular administration of saline as a control. Myositis in mice was induced for 10 hours before left and right

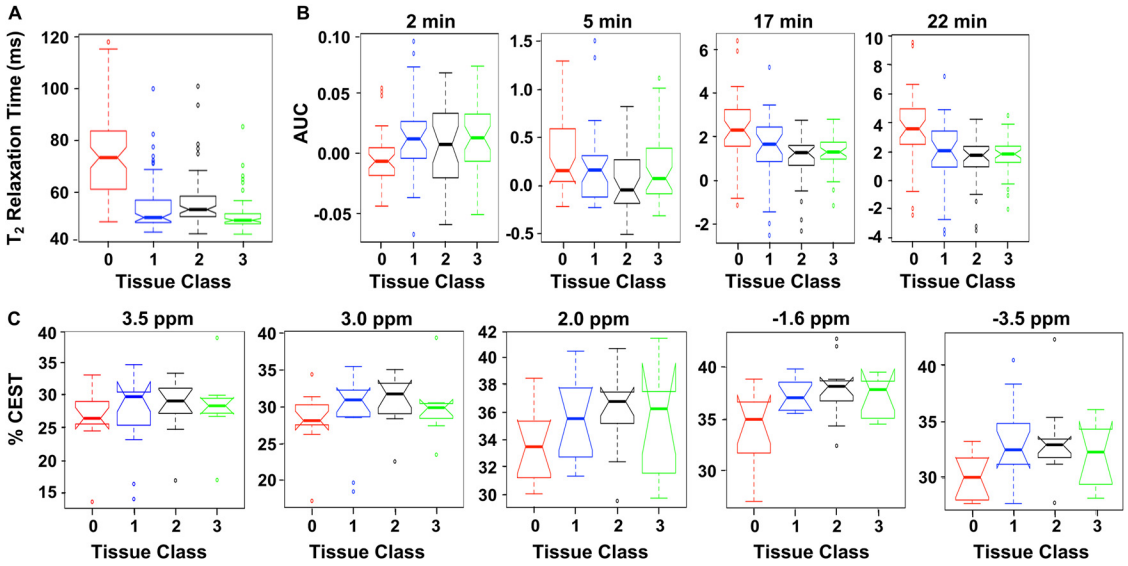

Figure 2. Distributions of magnetic resonance imaging (MRI) results in notched boxplot representations. 0 = infected tissue class (red); 1 = normal muscle on left thigh tissue class (blue); 2 = inflamed tissue class (black); and 3 = normal muscle on right thigh tissue class (green). The distributions of T_2 relaxation times for the 0, 1, 2, and 3 tissue classes (A). The area under the curve (AUC) from injection to 2 minutes (left), 5 minutes (second from left), 17 minutes (second from right), and 22 minutes (right), respectively, for the 0, 1, 2, and 3 tissue classes (B). The distributions of %CEST signals at saturation frequencies of 3.5, 3.0, 2.0, −1.6, and −3.5 ppm for 0, 1, 2, and 3 tissue classes (C).

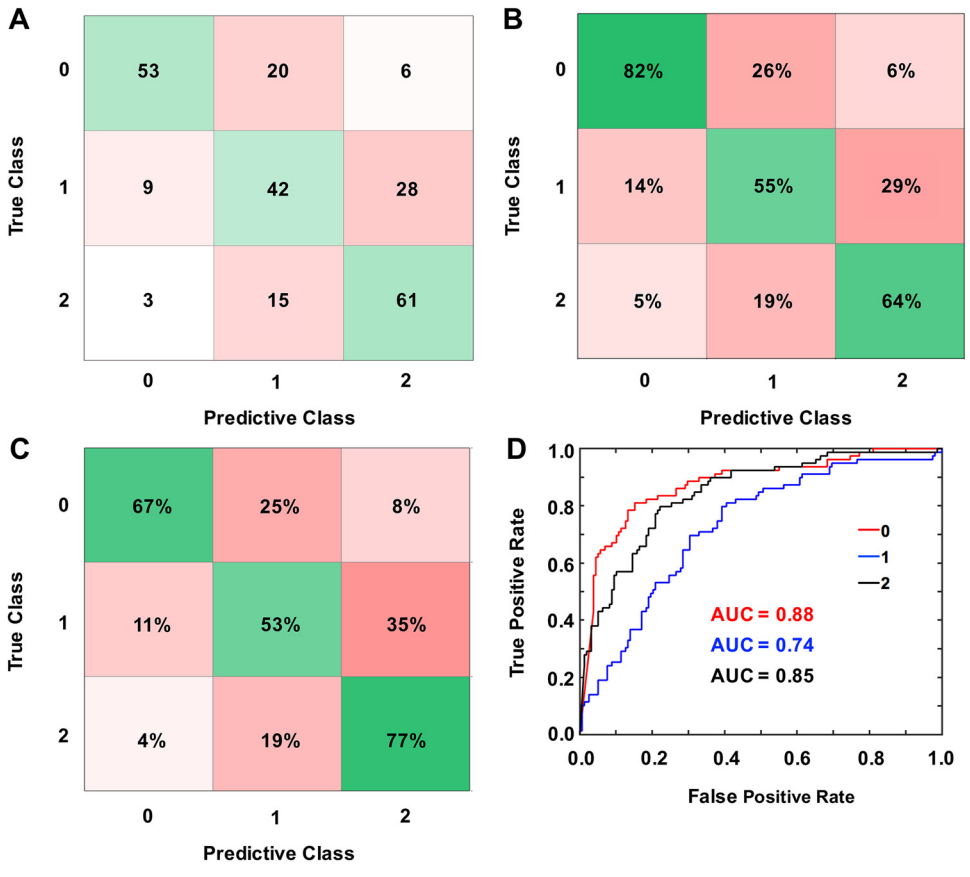

Figure 3. Error matrix representations after machine learning classification with a medium Gaussian support vector machine (MG SVM) algorithm using T_2 relaxation times as predictors. 0 = infected tissue class (red); 1 = inflamed tissue class (blue); and 2 = normal muscle on right thigh tissue class (black). Number of correct (green) and incorrect (red) predicted observations (A). Positive predictive value rates (green) and false discovery rates (red) (B). True-positive rates (green) and false-negative rates (red) (C). AUC for the receiver operator characteristic (ROC) curves represents classifier algorithm prediction accuracy (D).

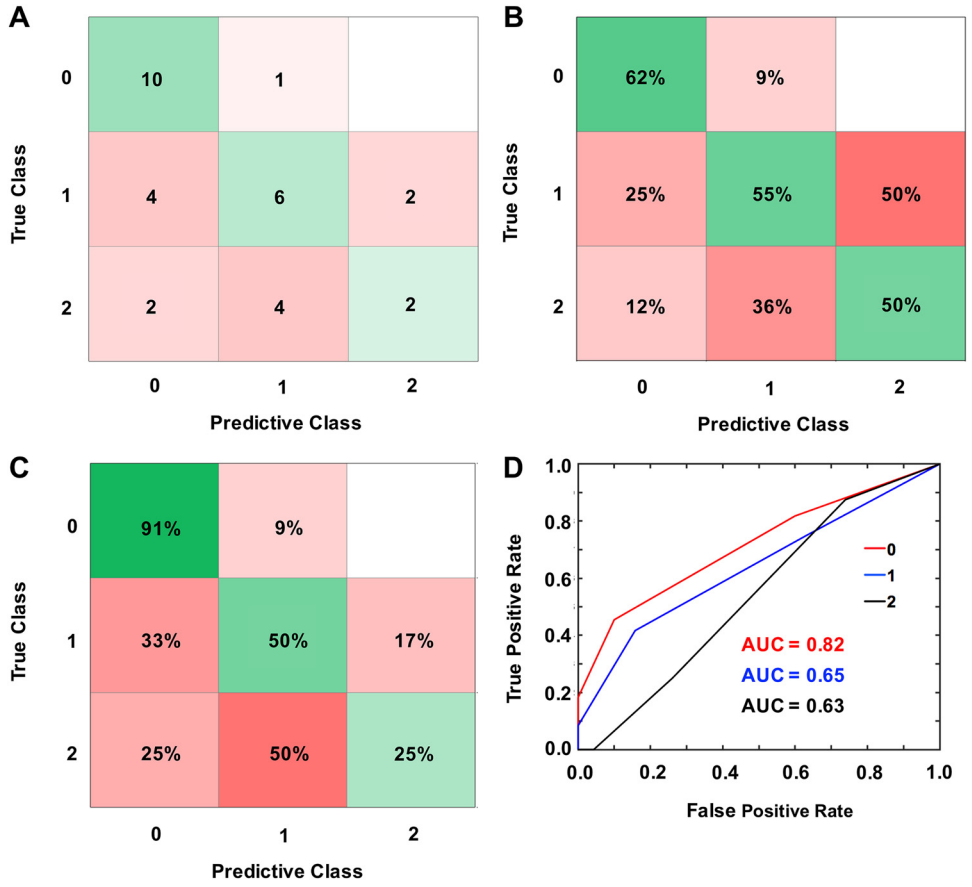

Figure 4. Error matrix representations after machine learning classification with a k-nearest neighbor algorithm using principal components from entire CEST spectra as predictors. 0 = infected tissue class (red); 1 = inflamed tissue class (blue); 2 = normal muscle on right thigh tissue class (black). Number of correct (green) and incorrect (red) predicted observations (A). Positive predictive value rates (green) and false discovery rates (red) (B). True-positive rates (green) and false-negative rates (red) (C). AUC for the ROC curves represents classifier algorithm prediction accuracy (D).

thigh tissue samples were harvested for staining and bacterial burden calculations. Tissue samples and microscope slides were prepared for H&E and Gram stains using the HistoCore Arcadia H (Leica, Wetzlar, Germany), and microscopic imaging was conducted on an Olympus BX50 L98-029 with an Olympus DP72 camera (Shinjuku, Tokyo, Japan) (Figure 6).

RESULTS

Twenty mice were successfully imaged 6–12 hours after induction of myositis. No mice expired following each 50-min imaging scan. The T_2-weighted MRI signals of the ROIs (Figure 1C) were higher for both the infected and inflamed tissues (tissue classes 0 and 2 in Figures 1 and 2) than for the normal tissues that appeared almost identical (tissue classes 1 and 3 in Figures 1 and 2). The CEST spectra of the tissue ROIs showed a significant decrease in water signal between −1.5 and −4 ppm owing to the relayed nuclear overhauser effect of aliphatic protons on proteins and lipids (Figure 1B; 38, 39). The DCE-MRI %SNR (signal-to-noise ratio) evolutions showed a clear difference between the infected and inflamed tissues from normal tissue (Figure 1D).

Boxplots of T_2 relaxation time for each tissue class showed that the infected tissues were statistically different for both the normal and inflamed tissue classes (Figure 2A; Table 1). A rank-sum test analysis was performed on the distribution of T_2 relaxation times to attain statistically significant differences ($P < .01$) between all tissue classes, except for the comparison of both normal tissues as expected ($P = .374$) (Table 1). Therefore, T_2 relaxation times can differentiate infected tissue from both inflamed and normal tissue, and can also differentiate inflamed tissue from normal tissue. Clinical translation of these results will require care to perform quantitative T_2 measurements with sufficient accuracy to also produce statistically significant differences between tissue classes (40).

Boxplot analyses of %CEST results showed that the infected versus inflamed tissue classes, and infected versus normal tissue classes, had statistically different %CEST signals at −1.6 and −3.5 ppm, and were not statistically different at 3.5, 3.0, and 2.0 ppm (Figure 2C; Table 1). A rank-sum test analysis was performed on the distribution of %CEST, which showed statistically significant differences ($P < .012$) between the infected tissue class and the other tissue classes for %CEST signals at both −1.6 and −3.5 ppm. The inflamed tissue class was not statistically different from either of the normal tissues, and both normal tissues were not statistically different from each other, at any saturation frequency. Therefore, CEST-MRI can differentiate infected tissue from inflamed and normal tissue, but it cannot differentiate inflamed tissue from normal tissue.

Relative K^{trans} and k_{ep} values were produced from the linear reference region model after pharmacokinetic analysis of DCE-MRI data. However, statistical significance was not achieved between all comparisons of 2 tissue classes (data not shown). Boxplot analyses of DCE CNR evolution showed no statistical significance between all tissue classes when results were analyzed for 1 minute and 5 minutes after injection and infusion of maltose (Figure 2B; Table 1). The infected tissue class showed

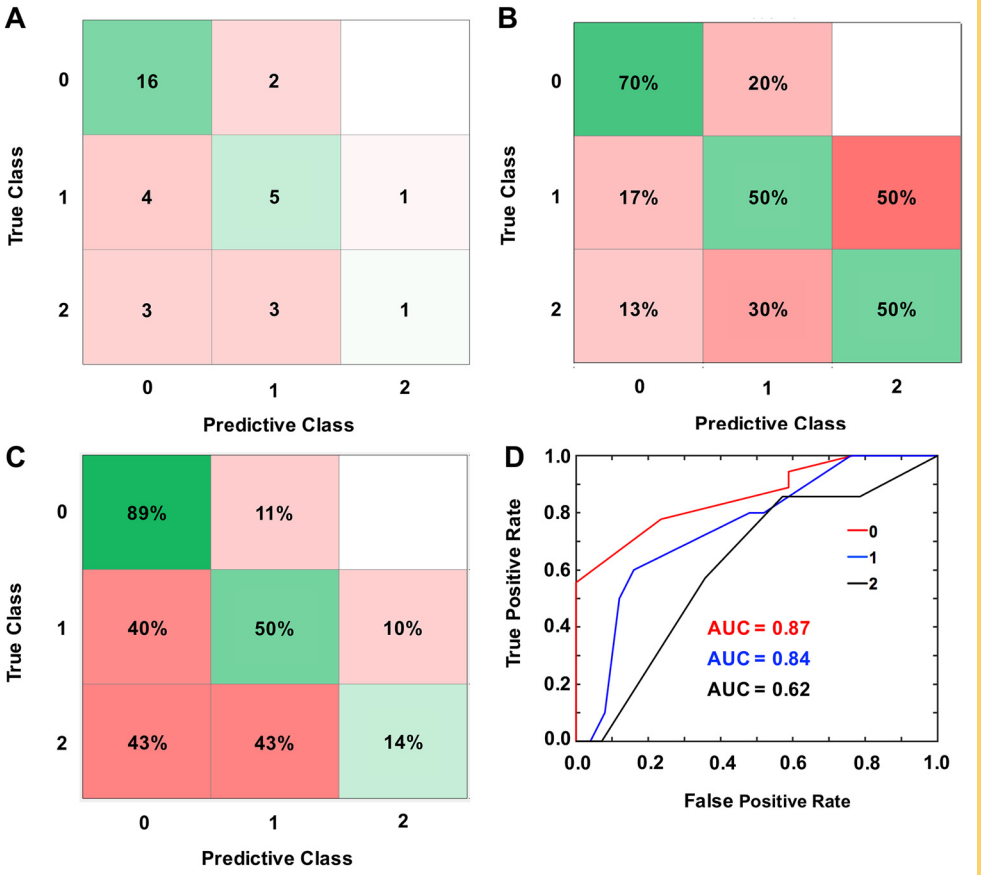

Figure 5. Error matrix representations after machine learning classification with a k-nearest neighbor algorithm using principal components from entire DCE pharmacokinetic curves as predictors. 0 = infected tissue class (red); 1 = inflamed tissue class (blue); 2 = normal muscle on right thigh tissue class (black). Number of correct (green) and incorrect (red) predicted observations (A). Positive predictive value rates (green) and false discovery rates (red) (B). True-positive rates (green) and false-negative rates (red) (C). AUC for the ROC curves represents classifier algorithm prediction accuracy (D).

statistical significance when compared to tissue classes 1, 2, and 3 after results were analyzed for 17 and 22 minutes after injection and infusion of maltose. Similarly, inflamed tissue class 2 was statistically different from both normal tissue classes 1 and 3, following injection and infusion of maltose after 17 and 22 minutes, respectively. The rank-sum test analysis was performed on the entire DCE-MRI data set to attain statistically significant differences ($P < .01$) between all tissue classes, except for the comparison of both normal tissues (Table 1). We included the first 10 minutes of baseline scans to serve as a negative control. These results showed that the AUC analysis of DCE-MRI results can differentiate infected tissue from both inflamed and normal tissue.

The Gaussian SVM with a medium kernel scale had the best performance among the classification models tested when T_2 relaxation times were used as predictors (data not shown). The complexity of a four-class machine learning classification dictated the need to use three tissue classes (0 = infected, 1 = inflamed, and 2 = normal left thigh tissue; Figure 3; see online supplemental Table S1). The model classified 82% of the infected tissue, and it classified a relatively poor 55% of the inflamed tissue, and 64% of the normal left thigh tissue (Figure 3C). The AUC of the ROCs ranged from 0.74 to 0.88 for the models, indicating good classification of both infected and normal tissue (Figure 3D; see supplemental Table S1). However, machine learning did not further improve the ability to classify each tissue class relative to boxplot analyses of T_2 relaxation time value distributions (Figure 2A).

The CEST spectra provided 101 predictors for classifying tissues (corresponding to each saturation frequency from −8 to 8 ppm, and excluding 9 predictors from −55 to −50 ppm). PCA using a k-nearest neighbors algorithm, resulted in a 91% correct

Table 1. Wilcoxon Rank-Sum *P*-values for the Distributions of T_2 Relaxation Time, %CEST, and AUC of the DCE CNR Evolutions Between Each Tissue Class

Imaging Technique[a]	0 & 1	0 & 2	0 & 3	1 & 2	1 & 3	2 & 3
T_2	0.001	0.001	0.001	0.009	0.374	0.001
CEST	0.003	0.001	0.011	0.554	0.787	0.438
DCE	0.001	0.001	0.001	0.009	0.374	0.001

[a]0 = infection; 1 = normal muscle (right leg); 2 = sterile inflammation; 3 = normal muscle (left leg).

classification for the infected tissue class (Figure 4C; see supplemental Table S1). PCA reduced the CEST spectra to 5 components, where the first 2 components explained 60% and 30% of the classification. These 2 components resulted in a good AUC of the ROC with >0.82 true-positive rates for infected tissue classification. The AUC of the ROCs for inflamed and normal tissue were only 0.65 and 0.63, respectively (Figure 4D; see supplemental Table S1). Therefore, while machine learning (Figure 4) has utility for positive classification of the infected tissue, the results matched those relative to boxplot analyses of CEST at each saturation frequency (Figure 2C).

DCE CNR evolutions provided 32 predictors (corresponding to each image repetition). A k-nearest neighbor algorithm resulted in an 89% correct classification for the infected tissue class (Figure 5C; see supplemental Table S1). PCA reduction of the DCE data to 5 components resulted in the first 2 components explaining 93% and 6% of the classification. The components resulted in good AUC of the ROCs with true-positive rates of 0.87 and 0.84 for the infected and inflamed tissue classes, respectively, and a modest 0.62 for the normal tissue class (Figure 5D; see supplemental Table S1). Therefore, machine learning (Figure 5) generated correct classification of infected tissue that is comparable to the more traditional DCE-MRI analyses of the AUC for at least 17 minutes after injection of maltose.

To validate the mouse model, H&E and Gram staining histological experiments were performed with 6 additional immunocompetent CBA/J mice following imaging studies. After induction of myositis following 10 hours of agent exposure, mice were humanely sacrificed, and tissues were collected for bacterial load calculations and histology (Figure 6). When intramuscular injections without inflammatory agents were given, the muscle remained normal (Figure 6A). Myositis-induced sterile inflammation after intramuscular administration of LPS resulted in significant inflammation of the tissue (Figure 6B). Myositis-induced inflammation after intramuscular administration of heat-killed bacteria also showed substantially inflamed tissue (Figure 6C). Finally, myositis-induced bacterial infection was clearly visualized after intramuscular injection of bacteria (Figure 6D). Bacterial burden ($\log_{10}$ CFU) was enumerated for mice with respect to exposure of inflammation-inducing LPS or heat-killed *E. coli*. The 3 mice exposed to LPS had an average bacterial burden of 6.95 ± 0.101, and the 3 mice exposed to heat-killed bacteria had an average bacterial burden of 6.56 ± 0.123 (Table 2).

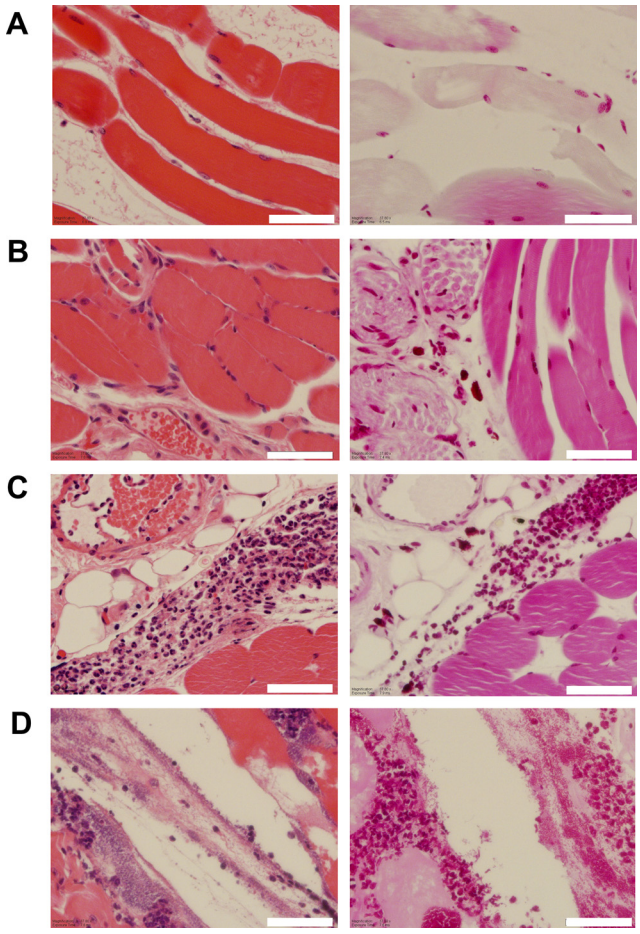

Figure 6. Hematoxylin and eosin (H&E) (left column) and Gram (right column) stains showing normal muscle (A), lipopolysaccharide (LPS)-induced inflammation (B), heat-killed *Escherichia coli* (*E. coli*)-induced inflammation (C), and Gram-negative bacteria (D). Scale bars on each image are 50 μm.

DISCUSSION

The high rate of positive classification of infected tissue from the other tissue classes was anticipated owing to the intrinsic differences between T_2 relaxation times of infected, inflamed, and normal muscle tissues at 7 T magnetic field strength (25). The addition of CEST-MRI and DCE-MRI did not provide additional information for improved classification and differentiation of infected and inflamed tissues. Our preliminary study provides a platform for future research that investigates the utility of T_2-weighted MRI for infection imaging and classification. Performing imaging studies with a larger cohort of mice and different bacterial models of myositis-induced infection and inflammation can further improve the repeatability and reproducibility of tissue classifications. We speculate that future studies can include a longitudinal evaluation of antibacterial treatment efficacy in mice with myositis infections, although further evidence of significant changes in T_2 after treatment are needed to warrant such studies. Nonetheless, T_2-weighted MRI is sufficient for evaluating and classifying infected and inflamed tissues, and it serves as an alternative to CEST and DCE-MRI when the administration of exogenous contrast agents is not needed.

The specific saturation frequencies of 3.5, 3.0, and 2.0 ppm were chosen to measure CEST arising from endogenous amide, amine, and hydroxyl groups, while −1.6 and −3.5 ppm were chosen to measure CEST arising from relayed NOE of aliphatic protons on proteins and lipids. Our results showed that machine learning did not improve overall classification of tissue models based on the entire CEST spectra, relative to classifications using the single saturation frequencies of −1.6 and −3.5 ppm. The classification of infected and inflamed tissues when CEST-MRI

Table 2. *Escherichia coli* Bacterial Burden (log_{10} CFU) in the Right Thighs of 6 Myositis-Induced Mice, Divided into 2 Groups of n = 3 Mice

	Bacterial Burden (log_{10} CFU)	
	Inflammatory Agent	
Mouse[a]	LPS	Heat-Killed *E. coli*
1	6.84	6.70
2	6.97	6.51
3	7.04	6.47
Average ± SD[b]	6.95 ± 0.101	6.56 ± 0.123

[a]3 mice were injected with inflammation-inducing LPS or heat-killed *E. coli* into the left thigh.
[b]SD = Standard Deviation

was analyzed with machine learning was expected to produce higher true-positive rates than we observed. However, similar CEST signal distributions for infected and inflamed tissues may contribute to the complexity of their overall classifications. The large influx of proteins and lipids associated with inflammation, whether induced via bacterial infection or sterile inflammation, appears to contribute to the significantly different CEST signal distributions at −1.6 and −3.5 ppm as compared with the statistically insignificant CEST signal distributions at 3.5, 3.0, and 2.0 ppm. These results are similar to other machine learning studies for T1-weighted relaxation MRI, CEST-MRI, and DCE-MRI that have been recently reported (24).

The classification of the tissue classes with the AUC from CNR evolutions of DCE-MRI was anticipated to produce a visibly separable distribution of AUC of infected tissue from the rest of the tissue classes because of the biologically relevant utility of maltose as a bacterial energy source (31, 33). The injection and infusion of maltose increases the specificity of T_2-weighted DCE-MRI of bacterial infections. These results indicate that maltose can be used as an exogenous contrast agent that can contribute to imaging infections, and it has potential to be combined with imaging bacteria-specific PET tracers during PET/MRI studies (41).

Contrary to our expected outcome of an increase in positive tissue classifications using PCA and machine learning, tissue classifications were adequate using the distribution of tissue T_2 relaxation times. We found that distributions of T_2 relaxation times, CEST signals at −1.6 and −3.5 ppm, and DCE CNR evolutions can be effectively used to classify tissue classes without machine learning. When using entire CEST spectra and DCE pharmacokinetic curves as predictors for PCA and machine learning, we achieved great classifications of infected tissue at 91% and 89%, respectively. However, PCA and machine learning failed to distinguish inflamed tissues from normal tissue classes, and did not further improve the successful classification of tissue models using the distributions of T_2 relaxation times, %CEST, and more simplistic analyses of DCE-MRI AUC in our studies.

Supplemental Materials

Supplemental Table 1: https://doi.org/10.18383/j.tom.2019.00009.sup.01

ACKNOWLEDGMENTS

We extend special thanks to Drs. Sanjay Jain and Alvaro Ordoñez of Johns Hopkins University for providing advice on bacterial culturing methods for in vivo imaging studies. We would also like to thank Gillian Paine-Murrieta and Betsy Dennison of the TACMASR facility for assisting us with tissue sample harvesting and H&E- and Gram-stained microscope slides. This work was supported by NIH grants R01CA169774, P30CA023074, and P50CA95060, and by the Institutional Research Grant number 128749-IRG-16-124-37-IRG from the American Cancer Society.

Disclosures: No disclosures to report.

Conflict of Interest: The authors have no conflict of interest to declare.

REFERENCES

1. Vincent JL. Increasing awareness of sepsis: World Sepsis Day. Crit Care. 2012; 16:152.
2. Sehnaz A, Akova M. Antibacterial resistance in patients with hematopoietic stem cell transplantation. Mediterr J Hematol Infect Dis. 2017;9:e2017002.
3. Yohei D, Bonomo RA, Hopper DC, Kaye KS, Johnson JR, Clancy CJ, Thaden JT, Stryjewski ME, van Duin D. Gram-negative bacterial infections: research priorities, accomplishments, and future directions of the antibacterial resistance leadership group. Clin Infec Dis. 2017;64:S30–S35.
4. Banin E, Hughes D, Kuipers OP. Editorial: bacterial pathogens, antibiotics, and antibiotic resistance. FEMS Microbiol Rev. 2017:41:450–452.
5. Tsalik EL, Bonomo RA, Folwer VG, Jr. New molecular diagnostic approaches to bacterial infections and antibacterial resistance. Ann Rev Med. 2018;69:379–394.
6. Gowrishankar G, Namavari M, Jouannot EB, Hoehne A, Reeves R, Hardy J, Gambhir SS. Investigation of 6-[^{18}F]-fluoromaltose as a novel PET tracer for imaging bacterial infection. PLoS One. 2014;9:e107951.
7. Namavari M, Gowrishankar G, Srinivasan A, Gambhir SS, Haywood T, Beinat C. A novel synthesis of 6-[^{18}F]-fluoromaltotriose as a PET tracer for imaging bacterial infection. J Label Compd Radiopharm. 2018;61:408–414.
8. Welling MM, Hensbergen AW, Brunschoten A, Velders AH, Roestenberg M, van Leeuwen FW. An update on radiotracer development for molecular imaging of bacterial infections. Clin Transl Imaging. 2019:7:105–124.
9. del Rosal T, Goycochea WA, Méndez-Echevarría A, García-Fernández de Villalta M, Baquero-Artigao F, Coronado M, Dolores Marín M, Albajara L. ^{18}F-FDG PET/CT in the diagnosis of occult bacterial infections in children. Eur J Pediatr. 2013;172:1111–1115.
10. Ohlsen K, Hertlein T. Towards clinical application of non-invasive imaging to detect bacterial infections. Virulence. 2018;9:943–945.
11. Thornton CR. Molecular imaging of invasive pulmonary aspergillosis using ImmunoPET/MRI: the future looks bright. Front Microbiol. 2018;9:691.
12. Kanao S, Kataoka M, Iima M, Ikeda DM, Toi M, Togashi K. Differentiating benign and malignant inflammatory breast lesions: value of T_2 weighted and diffusion weighted MR images. Magn Reson Imaging. 2018;50:38–44.
13. Katsuura Y, Cincere B, Cason G, Osborn J. Metastatic MSSA infection of the spine and extremities. BMJ Case Rep. 2018;2018:bcr-2017-222778.
14. Hirsch AJ, Roberts VHJ, Grigsby PL, Haese N, Schabel MC, Wang X, Lo JO, Liu Z, Kroenke CD, Smith JL, Kelleher M, Broeckel R, Kreklywich CN, Parkins CJ, Denton M, Smith P, DeFilippis V, Messer W, Nelson JA, Hennebold JD, Grafe M, Colgin L, Lewis A, Ducore R, Swanson T, Legasse AW, Axthelm MK, MacAllister R, Moses AV, Morgan TK, Frias AE, Streblow DN. Zika virus infection in pregnant rhesus macaques causes pacental dysfunction and immunopathology. Nat Commun. 2018;9:263.
15. Hooi WF, Malhotra A, Pollard J. Cytomegalovirus associated longitudinally extensive transverse myelitis and acute hepatitis in an immunocompetent adult. J Clin Neurosci. 2018;50:152–154.
16. Tawakol A, Sosnovik DE. PET/MR imaging of atherosclerosis: insights into atheroma structure and biology. JACC Cardiovasc Imaging. 2018;11:302–304.

17. Abid KA, Sobawale OA, Parkes LM, Naish J, Parker GJM, du Plessis D, Brough D, Barrington J, Allan SM, Hinz R, Parry-Jones AR. Assessing inflammation in acute intracerebral hemorrhage with PK11195 PET and dynamic contrast-enhanced MRI. J Neuroimaging. 2018;28:158–161.
18. Calcagno C, Lairez O, Hawkins J, Kerr SW, Dugas MS, Simpson T, Epskamp J, Robson PM, Eldib M, Bander I, Raman PK, Ramachandran S, Pruzan A, Kaufman A, Mani V, Ehlgen A, Niessen HG, Broadwater J, Fayad ZA. Combined PET/DCE-MRI in a rabbit model of atherosclerosis: integrated quantification of plaque inflammation, permeability, and burden during treatment with a leukotriene A4 hydrolase inhibitor. JACC Cardiovasc Imaging. 2018;11:291–301.
19. te Boekhorst BC, van Tillborg GA, Strijkers GJ, Nicolay K. Molecular MRI of inflammation in atherosclerosis. Curr Cardiovasc Imaging Rep. 2012;5:60–68.
20. Liu J, Bai R, Li Y, Staedtke V, Zhang S, van Zijl PCM, Liu G. MRI detection of bacterial brain abscesses and monitoring of antibiotic treatment using bacCEST. Magn Reson Med. 2018;80:662–671.
21. Liu G, Bettegowda C, Qiao Y, Staedtke V, Chan KWY, Bai R, Li Y, Riggins GJ, Kinzler KW, Bulte JWM, McMahon MT, Gilad AA, Vogelstein B, Zhou S, van Zijl PCM. Noninvasive imaging of infection after treatment with tumor-homing bacteria using chemical exchange saturation transfer (CEST) MRI. Magn Reson Med. 2013;70:1690–1698.
22. Sajda P. Machine learning for detection and diagnosis of disease. Annu Rev Biomed Eng. 2006;8:537–565.
23. Wernick MN, Yang Y, Brankov JG, Yourganov G, Strother SC. Machine learning in medical imaging. IEEE Signal Process Mag. 2010;27:25–38.
24. DeGrandchamp JB, Cárdenas-Rodríguez J. *A Machine-Learning Approach to Measuring Tumor pH Using MRI*. Tucson: The University of Arizona; 2017:1–13.
25. Theodorou DJ, Theodorou SJ, Kakitsubata Y. Skeletal muscle disease: patterns of MRI appearances. Br J Radiol. 2012;85:e1298–e1308.
26. Saab G, Thompson TR, Marsh GD. Multicomponent T_2 relaxation of *in vivo* skeletal muscle. Magn Reson Med. 1999;42:150–157.
27. Song X, Xu J, Xia S, Yadav NN, Lal B, Laterra J, Bulte JW, van Zijl PCM, McMahon MT. Multi-echo length offset varied saturation (MeLOVARS) method for improved CEST imaging. Magn Reson Med. 2015;73:488–496.
28. Zu Z, Xu J, Li H, Chekmenev EY, Quarles CC, Does MD, Gore JC, Gochberg DF. Imaging amide proton transfer and nuclear overhauser enhancement using chemical exchange rotation transfer (CERT). Magn Reson Med. 2014;72:471–476.
29. Zhang XY, Wang F, Afzal A, Xu J, Gore JC, Gochberg DF, Zu Z. A new NOE-mediated MT signal at around −1.6 ppm for detecting ischemic stroke in rat brain. Magn Reson Imaging. 2016;34:1100–1106.
30. Zaiss M, Windschuh J, Goerke S, Paech D, Meissner JE, Burth S, Kickingereder P, Wick W, Bendszus M, Schlemmer HP, Ladd ME. Downfield-NOE-suppressed amide-CEST-MRI at 7 Tesla provides a unique contrast in human glioblastoma. Magn Reson Med. 2017;77:196–208.
31. Freundleim S, Ehmann U, Boos W. Facilitated diffusion of p-nitrophenyl-alpha-D-maltohexaoside through the outer membrane of Escherichia coli. Characterization of LamB as a specific and saturable channel for maltooligosaccharide. J Biol Chem. 1988;263:314–320.
32. Reuss R, Ludwig J, Shirakashi R, Ehrhart F, Zimmermann H, Schneider S, Weber MM, Zimmermann U, Schneider H, Sukhorukov VL. Intracellular delivery of carbohydrates into mammalian cells through swelling-activated pathways. J Membr Biol. 2004;200:67–81.
33. Dippel R, Boos W. The maltodextrin system of Escherichia coli: metabolism and transport. J Bacteriol. 2005;187:8322–83231.
34. Gopal S, Berg D, Hagen N, Schriefer EM, Stoll R, Goebel W, Kreft J. Maltose and maltodextrin utilization by Listeria monocytogenes depend on an inducible ABC transporter which is repressed by glucose. PLoS One. 2010;5:e10349.
35. Shah T, Lu L, Dell KM, Pagel MD, Griswold MA, Flask CA. CEST-FISP: a novel technique for rapid chemical exchange saturation transfer MRI at 7T. Magn Reson Imaging. 2013;31:497–507.
36. Liu G, Li Y, Sheth VR, Pagel MD. Imaging in vivo extracellular pH with a single paramagnetic chemical exchange saturation transfer magnetic resonance imaging contrast agent. Mol Imaging. 2012;11:47–57.
37. Cárdenas-Rodríguez J, Howison CM, Pagel MD. A linear algorithm of the reference region model for DCE-MRI is robust and relaxes requirements for temporal resolution. Magn Reson Imaging. 2013;31:497–507.
38. Wang F, Zu Z, Wu R, Wu TL, Gore JC, Chen LM. MRI evaluation of regional and longitudinal changes in Z-spectra of injured spinal chord of monkeys. Magn Reson Med. 2018;79:1070–1082.
39. Jones KM, Pollard AC, Pagel MD. Clinical applications of chemical exchange saturation transfer (CEST) MRI. J Magn Reson. 2018;47:11–27.
40. Ma D, Gulani V, Seiberlich N, Liu K, Sunshine JL, Duerk JL, Griswold MA. Magnetic resonance fingerprinting. Nature. 2013;495:187–192.
41. Weinstein EA, Ordonez AA, DeMarco VP, Murawski AM, Pokkali S, MacDonald EM, Klunk M, Mease RC, Pomper MG, Jain SK. Imaging Enterobacteriaceae infection *in vivo* with 18F-fluorodeoxysorbitol positron emission tomography. Sci Transl Med. 2014;6:259ra146.